# Assessing riverbank erosion in Bangladesh using time series of Sentinel-1 radar imagery in the Google Earth Engine

Jan Freihardt[1] & Othmar Frey[2,3]

[1]Centre for Comparative and International Studies (CIS), ETH Zurich, 8092 Zurich, Switzerland
[2]Institute of Environmental Engineering, ETH Zurich, 8093 Zurich, Switzerland
[3]Gamma Remote Sensing, 3073 Gümligen, Switzerland

*Correspondence to*: Jan Freihardt (jan.freihardt@ir.gess.ethz.ch)

**Abstract.** Riverbank erosion occurs along many of the Earth's river systems, affecting riverine populations by destroying agricultural land and housing. In this study, we detected past events of riverbank erosion along the Jamuna River in Bangladesh using time series of Sentinel-1 satellite radar imagery, ground range detected (GRD) data with a 12-day revisit cycle, available in the Google Earth Engine (GEE). Eroded land is detected by performing a land cover classification and by detecting land cover changes from vegetated areas before the monsoon to sand or water after the monsoon. Further, settlements are detected as persistent scatterers, and classified as eroded if they are located on eroded land. We found that with Sentinel-1 data, erosion locations can be determined already one month after the end of the monsoon, and hence potentially earlier than using optical satellite images which depend on cloud-free daylight conditions. Further, we developed an interactive GEE-based online tool allowing the user to explore where riverbank erosion has destroyed land and settlements along the Jamuna in five monsoon seasons (2015-2019). The source code of our implementation is publicly available, providing the opportunity to reproduce the results, to adapt the algorithm and to transfer our results to assess riverbank erosion in other geographical settings.

## 1 Introduction

In Bangladesh, located in one of the largest river deltas of the world (Misachi, 2017), riverbank erosion is among the most drastic environmental processes in terms of yearly damage. Around 20 out of 64 districts in Bangladesh are prone to riverbank erosion, which consumes around 8.700 ha of land each year and thereby affects around 200.000 people by destroying their house and/or their agricultural land (Alam, 2017). Large-scale erosion – whereby several hundred square meters of land can collapse into the river within short time – mainly happens during the rainy monsoon season typically from June to October. Such erosion events occur primarily in a limited number of hotspot areas along the three major streams of Bangladesh, Jamuna, Ganges and Meghna.

In this study, we focus on the Jamuna River since first, it is one of the most dynamic river systems in the world, eroding several square kilometers of land each year (Oberhagemann et al., 2020; Hassan et al., 2017; Khan et al., 2022; Pahlowan and Hossain, 2015). The Jamuna is among the largest braided river systems in the world, forming various channels at a total width of around 12 km (Sarker et al., 2014). Since the 1970s, its bank line has shifted by around 20 km, continuously eroding the riverbank and creating new land, mainly in the form of islands (Dixon et al., 2018; Mount et al., 2013). Second, from a societal point of view, this large-scale erosion has significant impacts on the livelihoods of the populations living along the river, leading to economic hardship and human displacement (Alam et al., 2019; Alam, 2017; Ferdous et al., 2019). Hence, advancing the available tools to assess erosion along the Jamuna appears of utmost importance.

Each year, the Bangladesh Water Development Board (BWDB) commissions an assessment of last year's erosion based on optical satellite imagery (e.g. CEGIS, 2018). This report is usually available only a few weeks before the beginning of

the monsoon season, that is in May. This is due to the dependence of the analysis on cloud-free optical images, which are available in November/December for certain years, but only in January for other years. There is, thus, a need to establish an erosion assessment that is independent of cloud conditions and potentially available earlier, which would give communities along the rivers more time to prepare for the upcoming monsoon season.

In general, two distinct approaches exist to assess riverbank erosion quantitatively. First, the river system can be simulated using morphological numerical models. The capacities of such models increased significantly with the development of more powerful computers in the 2000s (Williams et al., 2016; Langendoen and Simon, 2008; Luppi et al., 2009). Computing power is necessary since fluvial systems are highly complex due to the large number of processes, scales and dimensions involved. Applying a numerical model to a river system as complicated as a braided river, however, would be extremely difficult, if not impossible. Indeed, one study that modelled erosion along the Jamuna River numerically did so for only 8 out of the 250 kilometers total length (Islam and Matin, 2022).

The second approach to assess erosion at the large spatial scale of entire river systems is remote sensing, using either passive or active systems. Passive optical systems are widely used and serve a variety of purposes. One important application is the classification of land cover (Trianni et al., 2014; Du et al., 2016; Rishikeshan and Ramesh, 2018; Donovan et al., 2019; Immitzer et al., 2016). A second field of application is the monitoring of earth system processes, such as quantifying and mapping riverbank erosion and accretion along the Ganges (Hossain et al., 2013), the Yellow River (Chu et al., 2006), the Mekong (Kummu et al., 2008), and the Jamuna and Padma Rivers in Bangladesh (Islam, 2009). Lastly, they can also help to generate hazard and risk maps, for instance, for landslide hazard (Joyce et al., 2009) or flood risk (El-Behaedi and Ghoneim, 2018).

Passive optical systems rely on receiving reflected sunlight from the Earth's surface which leads to a significant drawback: They cannot image the Earth's surface at night or under cloudy conditions. While the former is problematic mainly for rapidly occurring events such as floods or storms, the latter can affect any application, especially in cloud-prone regions. For land cover classification or monitoring of slowly occurring phenomena such as glacier movement or land cover change, cloud coverage of individual images can usually be compensated by information from cloud-free images obtained at earlier or later times. Yet, this strategy does not work if cloud coverage is continuous for a prolonged period. This is the case in Bangladesh, where cloud coverage is high during the monsoon season lasting for months.

Active microwave sensors such as lidar and radar emit a signal themselves and measure the radiation that is reflected from the target. Today, the most important imaging radar technology used in remote sensing applications is Synthetic Aperture Radar (SAR) which provides high-resolution two-dimensional images independent from daylight, cloud coverage and weather conditions (Moreira et al., 2013).

Similar to optical systems, radar systems are employed in a wide range of applications. Examples include the extraction of shorelines (Al Fugura et al., 2011) and rivers (Sghaier et al., 2017), mapping of open water bodies (Santoro and Wegmuller, 2014), or land cover classification (Cable et al., 2014). On the topic of natural disasters, extensive research has investigated the use of radar for mapping the extent and depth of floods, for instance in the Amazon (Martinez and Le Toan, 2007), the USA (Townsend, 2001), Taiwan (Chung et al., 2015), as well as for monsoon flooding in Bangladesh (Imhoff et al., 1987). Further, several studies used SAR data for fully automated flood detection to provide near-real time disaster information (Martinis et al., 2009; Martinis et al., 2015; Twele et al., 2016). Thus, time series of spaceborne SAR images are potentially suitable to detect riverbank erosion and are, with Sentinel-1, available with short temporal sampling (6- or 12-days repeat-pass) on a continental to global scale.

In this paper, we present a feasibility study on riverbank erosion assessment based on time series of Sentinel-1 SAR imagery. Our study area is the Jamuna River in Bangladesh, for which a large-scale erosion assessment based on radar – and hence independent of cloud or weather conditions – has not been done yet. Given the severe impacts that riverbank erosion has each year on populations residing along the Jamuna, advancing the available tools to assess erosion appears important not only from an academic, but also from a practical perspective. We employ a radar backscatter based detection of specific locations affected by riverbank erosion and we quantify their spatial extent for both eroded farmland and eroded settlements. The quality of the classification is evaluated with cloud-free Sentinel-2 optical data. We also assess 1) the "time to detection" after the monsoon and 2) the spatial resolution of the erosion detection, both of which are crucial parameters for potential emergency response and damage assessments. Given that the algorithm developed in this study is publicly available, it can potentially be transferred and adapted to other geographical settings at comparatively low effort and cost.

## 2 Methods and Data

### 2.1 The Google Earth Engine

A free and thus very attractive platform for analyzing remote sensing data is the Google Earth Engine (GEE). The GEE is a cloud-based platform providing access to a wide range of publicly available remote sensing data in connection with Google's massive cloud computing resources (Gorelick et al., 2017). The platform can be accessed free of charge by scientists, practitioners and other non-commercial users. Since its introduction in 2017, the GEE has been used for many remote sensing based (research) projects including applications close to the topical focus (e.g. mapping floods (Liu et al., 2018) or wetland dynamics (Muro et al., 2019)) or geographic focus of this work (e.g. monitoring rice growth in West Bengal (Mandal et al., 2018) or Bangladesh (Singha et al., 2019)).

Using the GEE is appealing since it gives simple access to a vast amount of remote sensing data, which do not have to be downloaded locally, but are processed in the cloud. Further, the GEE is relatively easy to use and does not require special software on the user side. Therefore, it can be applied in operational settings with limited resources, be it in terms of finances or trained personnel. GEE code can be shared conveniently via one link. The algorithm developed in this study can thus be easily accessed and adapted by research institutes or government authorities in Bangladesh. For all these advantages, this study used the GEE for all analyses.

Due to its computing architecture, the GEE can process only the amplitude, but not the phase information of radar images. The amplitude value corresponds to the reflectivity of an area, such that targets with high backscatter appear as bright spots in the radar image and flat smooth surfaces as dark (Moreira et al., 2013). As such, amplitude values can for instance be used to classify land cover. Due to this limitation of the GEE, the method presented subsequently works with backscatter coefficients only.

### 2.2 Data and pre-processing

This study used publicly available satellite imagery from the European Space Agency's (ESA) Sentinel mission (for more details see ESA, 2020b), launched in 2014, which collects C-band SAR images of the entire Earth's surface with a 6- to 12-day revisit cycle. Optical images were obtained from ESA's Sentinel-2 mission launched in 2015 with a 2- to 3-day revisit cycle at mid-latitudes (ESA, 2020c).

The Copernicus Sentinel-1 SAR data [2014-2021] used in this study was accessed through the GEE. The level-1 ground-range detected (GRD) scenes available in the GEE have already been pre-processed by the GEE following the steps from

ESA's Sentinel-1 toolbox (Veci et al., 2014; Google Developers, 2020). Since Sentinel-1 collects SAR data at a variety of modes, polarizations and resolutions, the pre-processed images provided by the GEE were filtered before the analysis to create a homogenous subset of data:

- Acquisition mode: Interferometric Wide Swath (IW) mode was selected since it is the primary conflict-free mode providing the 6- to 12-day revisit cycle over land (ESA, 2020a).
- Resolution: The IW images were filtered to keep only high-resolution images (pixel spacing of 10x10 m).
- Incidence angle: To reduce backscatter variation, only images with a look angle between 30° and 45° were kept.
- Look direction (ascending/descending): The influence of both look directions was tested for the detection of settlements. For the land cover classification, the ascending orbit was chosen. The relative orbit number of all ascending and descending images was 114 and 150, respectively, ensuring identical imaging geometry for all images of a certain look direction. Per look direction, the revisit cycle was 12 days.
- Polarization: For the IW mode, VV and VH polarizations are available. Since VH is available only from 2017 on, all analyses were performed on VV images.

Figure 1 gives an overview of the steps taken to develop the erosion detection algorithm. Methodological details are explained in the following sections. The full code used to develop the classifiers for land cover and settlements is referenced in the section "Code availability".
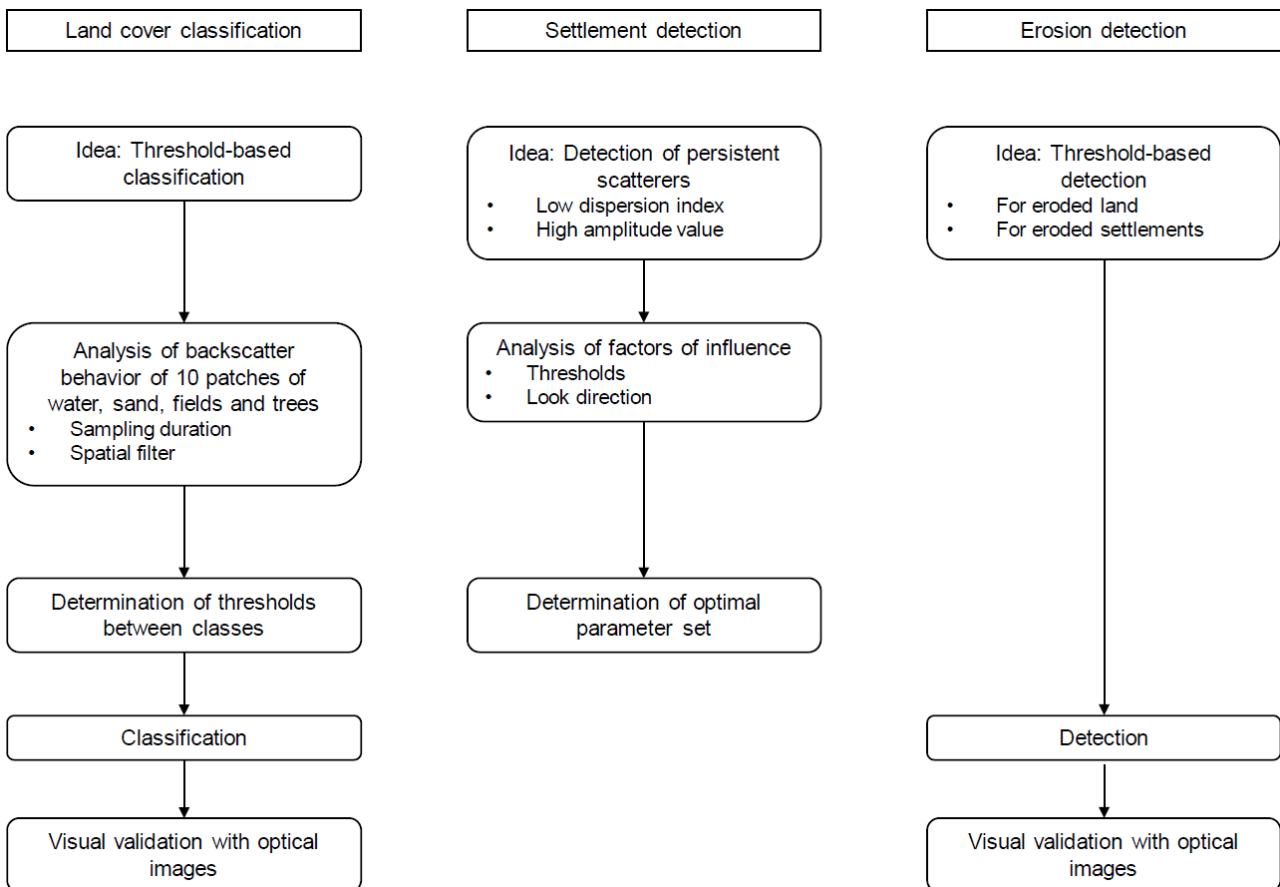
**Figure 1: Overview of the analytical strategy to develop an algorithm detecting eroded farmland and settlement.**

**2.3 Land cover classification**

To get a visual impression of the backscattering characteristics of different land cover types, the average backscatter coefficient of five classes (settlement, trees, fields, sand and water) was plotted for the period from January 2018 to

February 2020. For each of the four land cover classes water, sand, trees and agricultural fields, ten patches of size 100x100 m were chosen based on visual inspection of the optical satellite images provided by the GEE. For each class, the ten patches were distributed along the length of the Jamuna River. The locations of the patches are shown in Fig. A1.

140    The speckle inherent in SAR images can be reduced by temporal averaging (maintaining spatial resolution, but requiring several images) or by spatial filtering (requiring only one image, but reducing spatial resolution). There exists, thus, a tradeoff between keeping full spatial resolution and using only a few images. To assess riverbank erosion in Bangladesh, it would be ideal to use only a few images (to obtain the assessment as early as possible after the end of the monsoon season) while maintaining spatial resolution (to have a precise estimate of the erosion extent). Therefore, a compromise

145    has to be found between sampling duration and spatial resolution. We tested the influence of these two parameters for a range of configurations:

- Eight sampling durations: two weeks; 1 month; 2, 3, 4, 5, 6, 7 months. Each of these eight periods started on 01 November 2018. All images within the respective period were averaged temporally before the subsequent analysis.

150    - Seven spatial filters: no filter; 3x3 refined Lee filter; 3x3, 5x5, 7x7, 25x25 and 50x50 boxcar filter (Lee, 1981; Lee et al., 2009). The filters were applied to the absolute backscatter values.

For a certain imaging configuration (sampling duration and filter type), the mean backscatter as well as the standard deviation of the pixels within each patch were calculated. Subsequently, these ten patch-specific mean and standard deviation values were averaged to yield one mean backscatter and one standard deviation value per land cover class and

155    imaging configuration.

To classify pixels into one of the four classes, thresholds were defined between water/sand, sand/fields and fields/trees. The thresholds were calculated as $0.5 * \left[(mean_i + n * \sigma_i) + (mean_j - n * \sigma_j)\right]$ where $i$ and $j$ indicate the class with the lower and higher mean backscatter, respectively. $n$ was chosen as the largest natural number such that $(mean_i + n * \sigma_i)$ and $(mean_j - n * \sigma_j)$ would not overlap. $n$ could thus be different for each pair of classes. For trees, an additional upper

160    threshold was set at -2 dB to distinguish them from settlements. Pixels were classified according to their backscatter value with respect to these thresholds. For instance, a pixel with a backscatter value larger than the threshold water/sand, but smaller than the threshold sand/fields was classified as "sand". The quality of the classification was assessed visually using optical Sentinel-2 images.

### 2.4 Settlement detection

165    Since houses in rural Bangladesh are typically surrounded by trees, they are not fully visible on satellite images. Moreover, they cover only small areas compared to water, sand or farmland. Therefore, they cannot be well detected with the classification approach presented in Sect. 2.3, which involves spatial averaging.

To detect houses, we exploit the fact that unlike vegetation, houses do not move or change substantially over time. Due to this low temporal decorrelation, houses are treated as persistent scatterers (PS) (Ferretti et al., 1999). Detecting PS

170    candidates in radar images usually implies analyzing phase coherence, which cannot be done in GEE where only amplitude information is available. However, Ferretti et al. (2001) show that phase dispersion can be estimated from the amplitude dispersion index $\sigma_A / m_A$ where $m_A$ and $\sigma_A$ are the mean and the standard deviation of the amplitude values, respectively. PS can then be selected by computing the dispersion index of each pixel from a stack of several SAR images of the same scene and keeping only those pixels exhibiting a low dispersion index. The typical range of threshold values

175    for the dispersion index goes from 0.25 (Ferretti et al., 2001) to 0.4 (van Leijen, 2014).

Houses are not the only structures than can have a low dispersion index. Bare surfaces, for instance, might also be relatively stable over time. Therefore, we combine the dispersion criterion with an amplitude threshold: Pixels are selected as PS candidates and hence houses if they show a low dispersion index and a high absolute backscatter over a series of radar acquisitions. Two implementations of the amplitude threshold were compared: First, following Kampes and Adam (2004), a pixel is selected as PS candidate if its normalized cross section $\sigma_0$ is above a threshold $N_2$ in at least $N_1$ images. These authors propose thresholds of -2 dB for $N_2$ and $0.65K$ for $N_1$, where $K$ is the number of radar acquisitions. Second, the amplitude threshold was applied to the mean of all SAR images in the stack, instead of the individual images.

The sensitivity of the settlement detection was tested for the following parameters:

- Thresholds: For the dispersion index, threshold values of 0.25 and 0.4 were tested. For the amplitude threshold, -4 dB, -2 dB and 0 dB were analyzed. These analyses were done for a sampling duration of six months starting 01 November 2019.
- Look direction: Since the roofs of buildings typically have a specific orientation, they are likely to have a stronger backscatter for one of the two look directions "ascending" or "descending". Therefore, these two types were compared.

**2.5 Erosion detection**

In examining the impact of riverbank erosion on human livelihoods along the Jamuna River, we are interested in two effects, which are treated separately: erosion of land (farmland or trees) and erosion of houses. Land was identified as eroded in one specific monsoon season if it was classified as "field" or "trees" before the monsoon season and as "sand" or "water" afterwards. Erosion to sand and erosion to water were not differentiated further since in both cases, the land cannot be used for agriculture anymore, which is the main effect we are interested in in this application.

For classifying the land, a sampling duration of six months (November to April) was used for all years from 2014/15 to 2018/19. For 2019/20, only the images from November 2019 were used to simulate the case that the erosion detection has to be performed already in December after the end of the monsoon. A 7x7 boxcar filter was applied to create smooth and continuous erosion bands. The threshold discriminating sand/water from fields/trees was -13.2 dB and -12.7 dB for the case where six months and one month of data were used, respectively (Table B1 and Table B2). To detect eroded settlements, a similar strategy was followed: A pixel was selected as settlement eroded during a specific monsoon season if it was classified as "settlement" before the monsoon and as "sand" or "water" afterwards. The final algorithm to detect eroded farmland and settlement is schematized in Fig. 2.
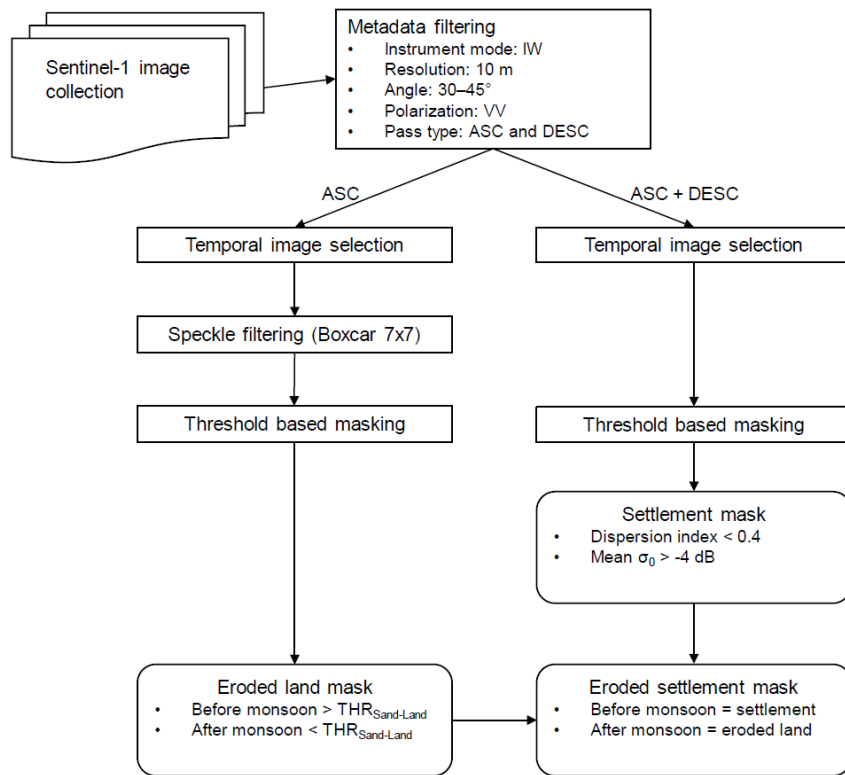
**Figure 2: Flow chart of the final implementation to detect eroded farmland and settlement. THR = threshold.**

### 2.6 Accuracy assessment

Since our study area is large (spanning more than 200 km from north to south), it was not feasible to collect sufficient ground-truth data to validate our land cover classification algorithm. To still be able to judge its accuracy, we compared the SAR-based classification to an independently conducted classification based on optical Sentinel-2 imagery, performed in the GEE.

Classification of Sentinel-2 images was based on the Normalized Difference Vegetation Index (NDVI). The NDVI takes on values between -1 and 1. In terms of the land cover classes relevant for our study, water bodies typically exhibit NDVI values below 0, bare ground between 0 and 0.1, and cultivated land above 0.1 (DeFries and Townshend, 1994; Huang et al., 2020).

Since the detection of eroded farmland relies only on the threshold between sand and vegetation (cf. Sect. 2.5), we differentiated only two landcover classes in the Sentinel-2 classification: sand/water (corresponding to all pixels exhibiting an NDVI value < 0.1) and vegetation/trees (corresponding to all pixels exhibiting an NDVI value > 0.1). While this is a large simplification, it serves the purposes of this study where we try to detect land that changes from vegetated before the monsoon to sand or water after the monsoon.

The pixel-level accuracy of the SAR-based classification was assessed for one site by counting all pixels which were a) identically classified as vegetation by both methods, b) "false positives" (classified as vegetation by the SAR-based method, and as sand/water by the Sentinel-2 based method), and c) "false negatives" (classified as sand/water by the SAR-based method, and as vegetation by the Sentinel-2 based method), respectively.

The quality of Sentinel-2 images depends on cloud cover. In Bangladesh, cloud cover varies seasonally, with highest values occurring during the monsoon (June to September) and lowest values in the dry season (November to March) (Fig. A2). Therefore, the accuracy assessment was performed for the two months with the lowest cloud cover (November and

March), using the one-month median NDVI value, respectively. For both November and March, the accuracy assessment was repeated for three consecutive years (2018/19 to 2020/21). The code for the Sentinel-2 based assessment is contained in the GEE code referenced in Sect. 2.2.

230 **3 Results**

**3.1 Determination of thresholds for land cover classification**

The average monthly backscatter of seven patches is shown as a time series in Fig. 3. The settlement and tree patch are the most stable since they are neither affected by (rapid) vegetation growth nor by monsoon flooding. The river patch has mostly the lowest coefficient, which increases during the monsoon, potentially due to wind and rain disturbing the flat

235 water surface. While fields generally have a backscatter coefficient close to that of trees, they can be seasonally flooded during the monsoon (field 2) or completely eroded (field 3). From the behavior of field 2, the dry season can be defined as the period between November and June of the following year (indicated by the vertical lines). The sand patch lies in between water and fields.
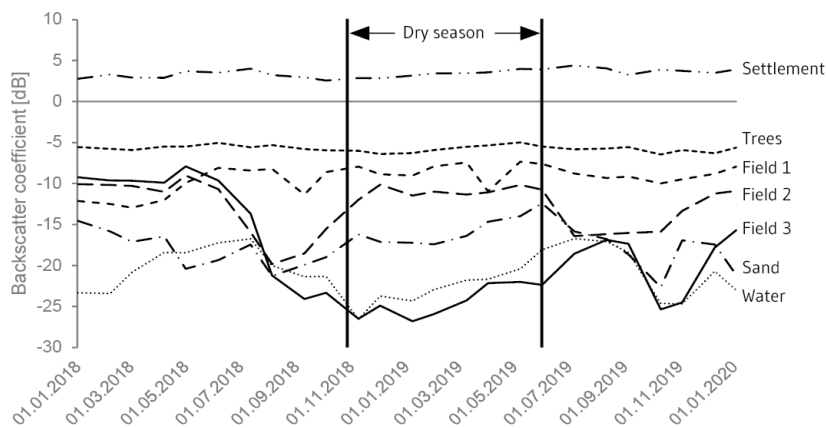
240 **Figure 3: Mean monthly backscatter of different land cover types (one patch per type; the location of the patches is shown in Fig. A1) between January 2018 and February 2020, obtained from C-band of Sentinel-1. Per month, between one and six images are averaged.**

The average backscatter of the ten sand patches is shown in Fig. 4a as a function of different sampling durations and filter configurations. For a given filter, there is no significant variation of the backscatter value with increasing sampling

245 duration. For a given sampling duration, the average backscatter increases slightly with increasing filter size. However, this increase becomes statistically significant at the 95 % level only for the largest filters (25x25 and 50x50 pixels). For such large filters (50x50 pixels corresponds to 500x500 meters), this is probably caused by other land cover classes with a higher backscatter value (e.g. fields) being included into the filter window.
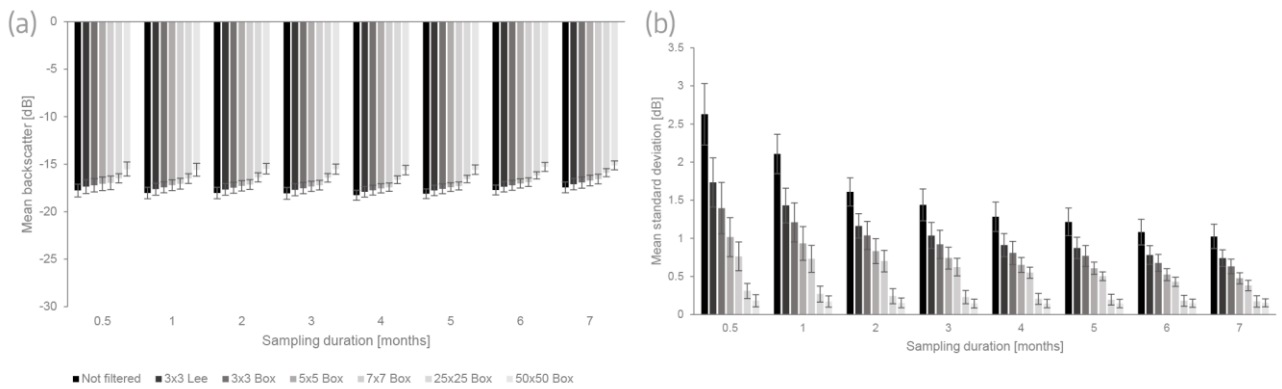
250

**Figure 4: Average backscatter (panel (a)) and average standard deviation (panel (b)) of the pixels within ten patches of sand for different sampling durations and filter sizes. Bars indicate the 95 % confidence interval. Lee – Lee filter. Box – boxcar filter.**

Figure 4b presents the standard deviation of all pixels within one patch, averaged over the ten sand patches. For a given

255    filter, the standard deviation decreases with increasing sampling duration. For a given sampling duration, it decreases with increasing filter size. These observations correspond to the two mechanisms for speckle reduction outlined in Sect. 2.3, namely temporal averaging and spatial filtering. The other three land cover classes "water", "fields" and "trees" show similar tendencies for filter size and sampling duration, both for average backscatter values and standard deviations (Fig. A3).

260    These findings allow defining thresholds to separate the four classes in the land cover classification. As discussed in Sect. 2.3, each combination of sampling duration and filter size has a certain advantage and a certain disadvantage. To illustrate this tradeoff, two extreme combinations are compared in Fig. A4. In practice, a compromise between these two extremes seems more likely, meaning that some spatial resolution has to be given up when a slightly longer sampling duration is used. One example for such a compromise is presented in Fig. 5, for which images from one month have been filtered

265    with a 3x3 boxcar filter.
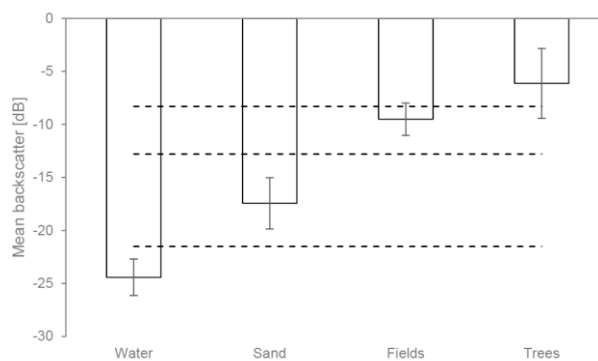
**Figure 5: Average backscatter for four land cover classes for a sampling duration of one month and a 3x3 boxcar filter. Bars indicate the mean ± 2 standard deviations. Horizontal lines indicate the thresholds between the respective classes.**

The determination of the thresholds is illustrated in Table 1 for the case of one month sampling duration and a 3x3 boxcar

270    filter. As can be seen in Fig. 5, the bars of fields and trees overlap if two standard deviations are used. However, they do not overlap if only one standard deviation is used. Hence, intervals with one standard deviation are used to determine the threshold between fields and trees. For water/sand and sand/fields, the intervals do not overlap even if three standard deviations are considered. Therefore, three standard deviations are used to calculate the respective thresholds. The thresholds for the two configurations from Fig. A4 are contained in Table B3 and Table B4. The average backscatter

 values shown in Table 1, Table B3 and Table B4 compare reasonably well to reference values from the literature (Table B5).

**Table 1: Determination of thresholds for a sampling duration of one month and a 3x3 boxcar filter. Values in bold are those that have been used to calculate the threshold indicated in the last column. All values are in dB. μ – mean. σ – standard deviation.**

|  | μ | σ | μ+σ | μ-σ | μ+2*σ | μ-2*σ | μ+3*σ | μ-3*σ | Threshold |
|---|---|---|---|---|---|---|---|---|---|
| Water | -24.4 | 0.9 | -23.6 |  | -22.7 |  | **-21.8** |  |  |
| Sand | -17.4 | 1.2 | -16.2 | -18.6 | -15.0 | -19.9 | **-13.8** | **-21.1** | -21.5 |
| Fields | -9.5 | 0.8 | **-8.8** | -10.3 | -8.0 | -11.0 | -7.2 | **-11.8** | -12.8 |
| Trees | -6.1 | 1.7 |  | **-7.8** |  | -9.4 |  | -11.1 | -8.3 |

Assuming the backscatter values in each class to be distributed normally around the mean, this approach allows an estimation of the accuracy of the resulting classification. In a normal distribution, 68 %, 95 % and 99.7 % of all values lie within "mean ± one, two and three standard deviations", respectively. As the thresholds "water-sand" and "sand-fields" are based on the interval with three standard deviations, we thus expect less than 0.15 % of all water pixels to be incorrectly classified as sand pixels. The same percentage applies for sand pixels being incorrectly classified as water/field pixels and for field pixels being misclassified as sand pixels. For "fields-trees", only one standard deviation has been used, and hence 16 % of all field/tree pixels are expected to be falsely classified as tree/field pixels, respectively.

Trees and fields can thus not be well distinguished in this setup, This shortcoming is, however, negligible in the context of studying riverbank erosion. Here, the focus is on land covered by fields or trees being eroded and appearing as sand or water afterwards. Therefore, the most important threshold is the one between sand and fields, which yields higher accuracy.

The classification resulting from these three imaging configurations is depicted in Fig. 6 with an optical Sentinel-2 image as the baseline. If only two weeks are sampled with a 25x25 boxcar filter, the spatial resolution is largely lost (top right). If, by contrast, no filter is applied and six months are sampled, the classification remains very fine-grained (bottom left). However, the distinction between sand and water is not very accurate. The compromise – one month sampling duration and a 3x3 boxcar filter (bottom right) – manages to preserve a large degree of spatial resolution while distinguishing well between the four classes. It thus seems the most appropriate of these three imaging configurations.
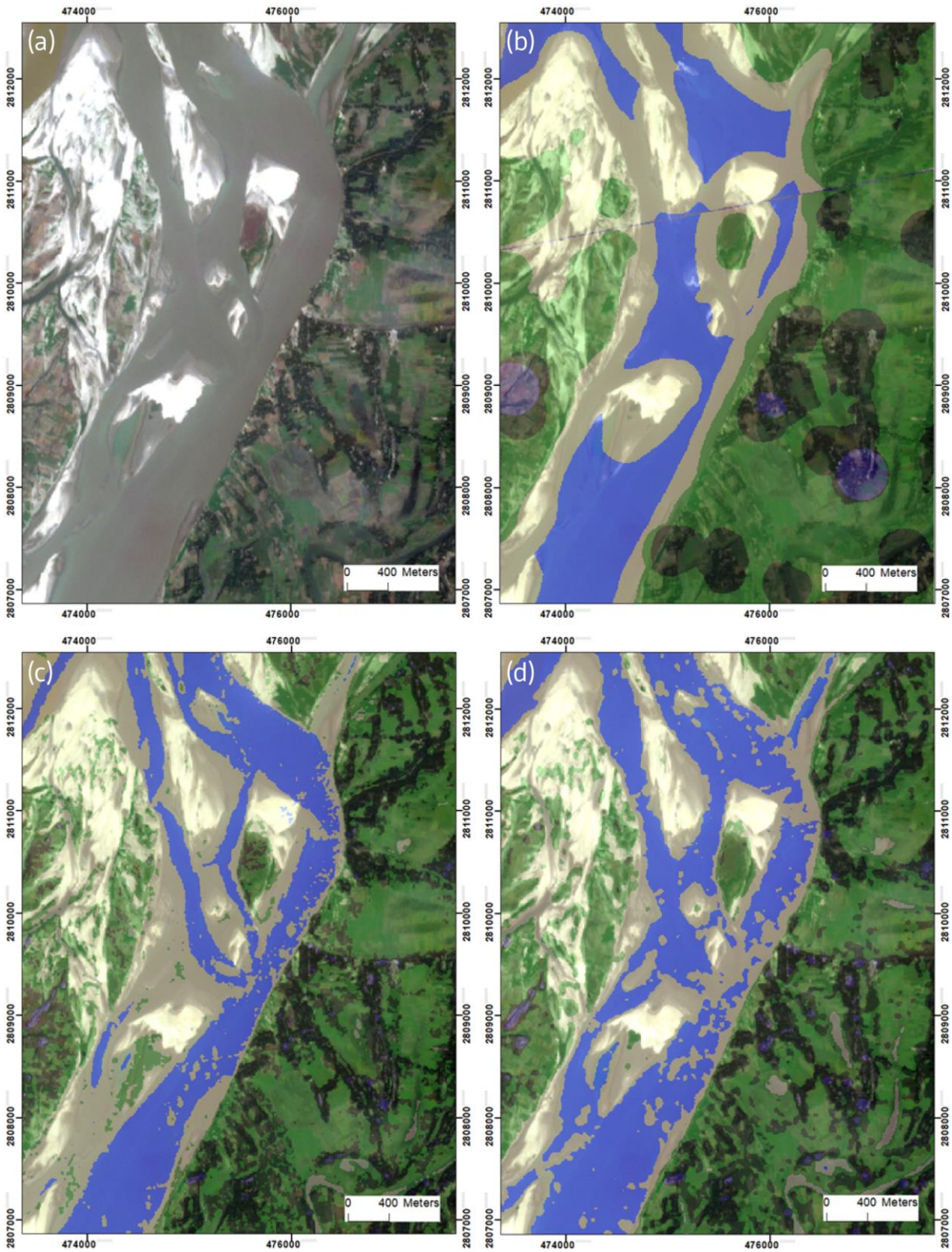
**Figure 6: (a) Sentinel-2 image of a stretch of the eastern riverbank of Jamuna River, taken in November 2019. Image dimensions: ca. 4.5x6 km. (b), (c) and (d) Classification result for a sampling duration of two weeks/25x25 boxcar filter, six months/no filter and one month/3x3 boxcar filter, respectively. Blue – water, sand – sand, light green – fields, dark green – trees. Source of optical background image: Sentinel-2. The location of the patch is shown in Fig. A1 (patch 1). Coordinates in this and all other maps are in "Gulshan 303 Bangladesh TM" (EPSG 3106).**

300

### 3.2 Detection of settlement as persistent scatterers

305 Figure A5a illustrates the need to apply an amplitude threshold in addition to the dispersion index. If only the dispersion index is used to classify settlements, many vegetation pixels that happen to be stable over the sampled time window are misclassified as settlements. The influence of the dispersion index threshold and the amplitude threshold is shown in Fig. 7. For the dispersion index, a threshold of 0.25 (panel (b)) selects only very stable pixels as PS candidates. Accordingly, less pixels are selected than for a threshold of 0.4 (panel (a)). For the amplitude threshold, the effect is the

310 opposite: Applying a threshold of -4 dB (red) selects more pixels as PS candidates than for -2 dB (blue) or 0 dB (orange). While the threshold of -4 dB thus seems to select more settlement pixels (e.g. upper left corner of panel (a)), also the risk of misclassifying tree pixels as settlements rises.

For our application, however, we are rather interested in detecting the rough location of settlements than in precisely distinguishing settlement and tree pixels. In fact, trees are often planted around houses, making them good indicators of

315 settlements. As too few settlement pixels are detected in panel (b), we suggest a threshold combination of 0.4 and -4 dB for the dispersion index and the amplitude, respectively. Still, it is important to note that even with this combination (red pixels in panel (a)), several pixels that appear as houses in the optical image are not detected. We should thus keep in mind that what the algorithm classifies as settlement is most likely indeed a settlement, but that it cannot detect all settlements, especially if they are covered by trees.

320 The influence of the look direction is illustrated in Fig. A5b. The overlap between the ascending and descending orbit is small. This corresponds to the fact that each building has a specific orientation of its roof. Therefore, some roofs have a stronger backscatter in the descending orbit, while others reflect more in the ascending orbit. Similar effects can be expected if persistent scatterers are located on walls or in corners of buildings. For maximum settlement detection, it is thus recommended to use SAR images of both look directions. To conclude, the recommended set of parameters to detect

325 settlements is to use an amplitude and dispersion index threshold of -4 dB and 0.4, respectively, using images of both ascending and descending orbit.
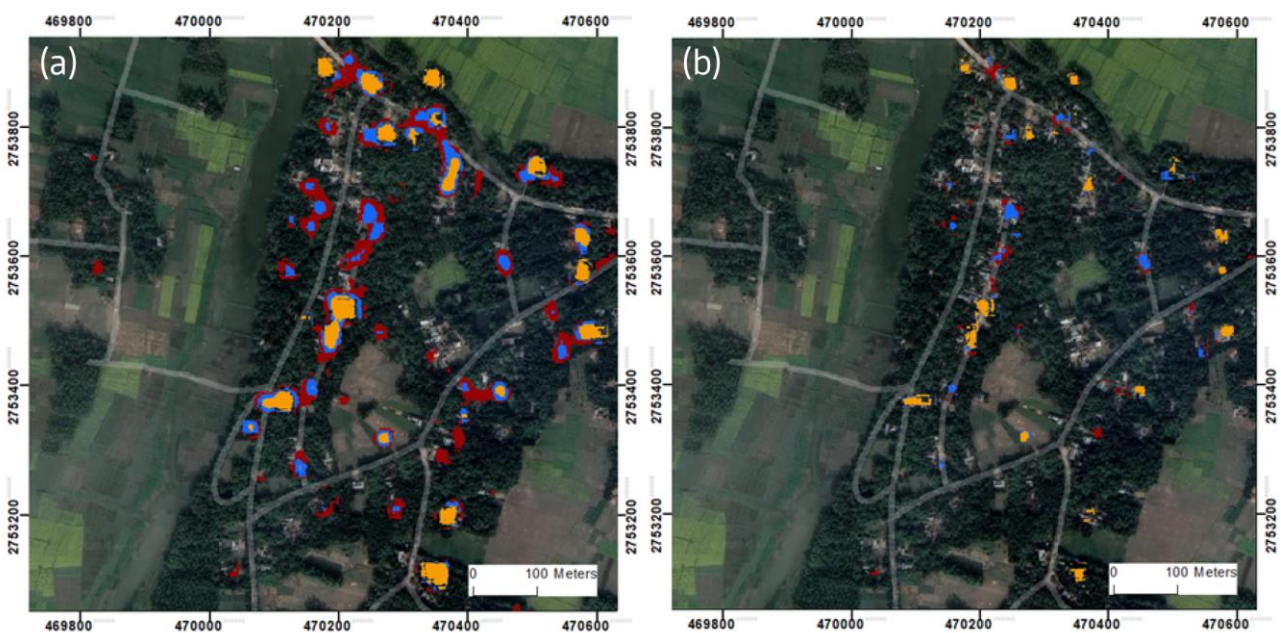
**Figure 7: Influence of classification thresholds on settlement detection. Shown are dispersion index thresholds of 0.4 (panel (a)) and 0.25 (panel (b)) – the lower the threshold, the more stable a pixel has to be for it to be classified as a PS candidate. Colors**
330 **correspond to different values of the amplitude threshold: -4 dB (red), -2 dB (blue), 0 dB (orange) – the lower the threshold,**

**the higher the chance of classifying tree pixels as settlement pixels. Source of optical background image: Google, ©2020 Maxar Technologies, CNES/Airbus.**

### 3.3 Detection of eroded farmland and settlements

Figure 9 illustrates the result of the erosion detection (both farmland and settlements) for one specific site for the monsoon seasons 2018 and 2019. To evaluate the quality of the erosion detection, the detected erosion patches are mapped on optical images from before and after the monsoon. The results of the overall validation of the land cover classification are contained in Sect. 3.4.

The focus of the project is on erosion occurring on the outer riverbanks of the Jamuna. Therefore, erosion happening on the sandbanks and islands in the river is omitted in the following discussion, which focuses exclusively on the long strip of eroded land on the outer riverbank. For both years, all that has been detected as eroded land has entirely been land before the monsoon (left column) and completely water after the monsoon (right column). For these examples, there is thus no type I error, i.e. classifying land as eroded when it is not.

There is, however, a type II error, i.e. eroded land that is not classified as such. This error tends to be small and thus negligible for the overall purpose of detecting sites where erosion occurred to a significant extent. Lastly, the algorithm can distinguish well between eroded farmland and eroded sand, as can be seen in the lower left corner of the 2019 image before the monsoon. Regarding the patches detected as eroded settlements (bright red), by far not all of the eroded settlement is detected. Again, this type II error is negligible given the purpose of detecting those sites that have seen erosion of settlement in general. For this, it is not necessary to detect every single house that has been eroded.

The erosion detection works for the monsoon seasons from 2015 to 2019, since Sentinel-1 images are only available from October 2014 onwards. Figure 9a shows the sequential nature of erosion, which does not occur at random locations, but typically in sites which have already experienced erosion during the previous monsoon season(s). We can also see the highly dynamic nature of land accretion and erosion. For instance, an island had formed at the place where land had been before the 2015 monsoon. Part of this island has been eroded again in the 2019 monsoon season (orange patch overlaying the dark brown 2015 erosion band). Further, settlements have been eroded in all five monsoon seasons (blue dots). Figure 9b shows where land was eroded in the 2019 monsoon along a larger section of the Jamuna River. Erosion occurred within, but to a large extent also outside of the hotspot areas predicted by CEGIS (2018).
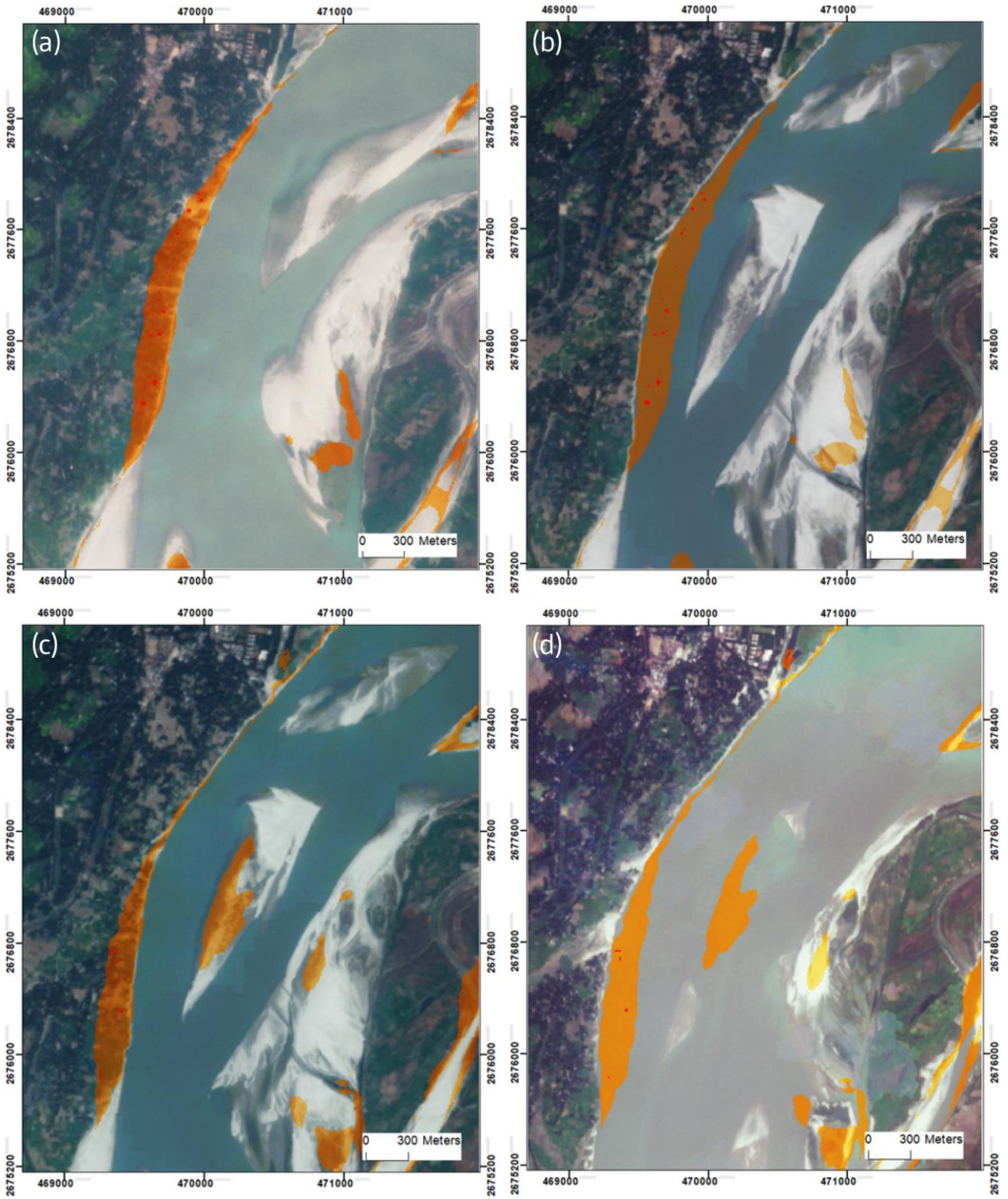
**Figure 8: Validation of erosion detection. Shown are eroded land (orange) and eroded settlements (red) for 2018 ((a) and (b)) and 2019 ((c) and (d)). Baseline: optical Sentinel-2 images from before ((a) and (c)) and after the monsoon ((b) and (d)). The location of the patch is shown in Fig. A1 (patch 3).**

360
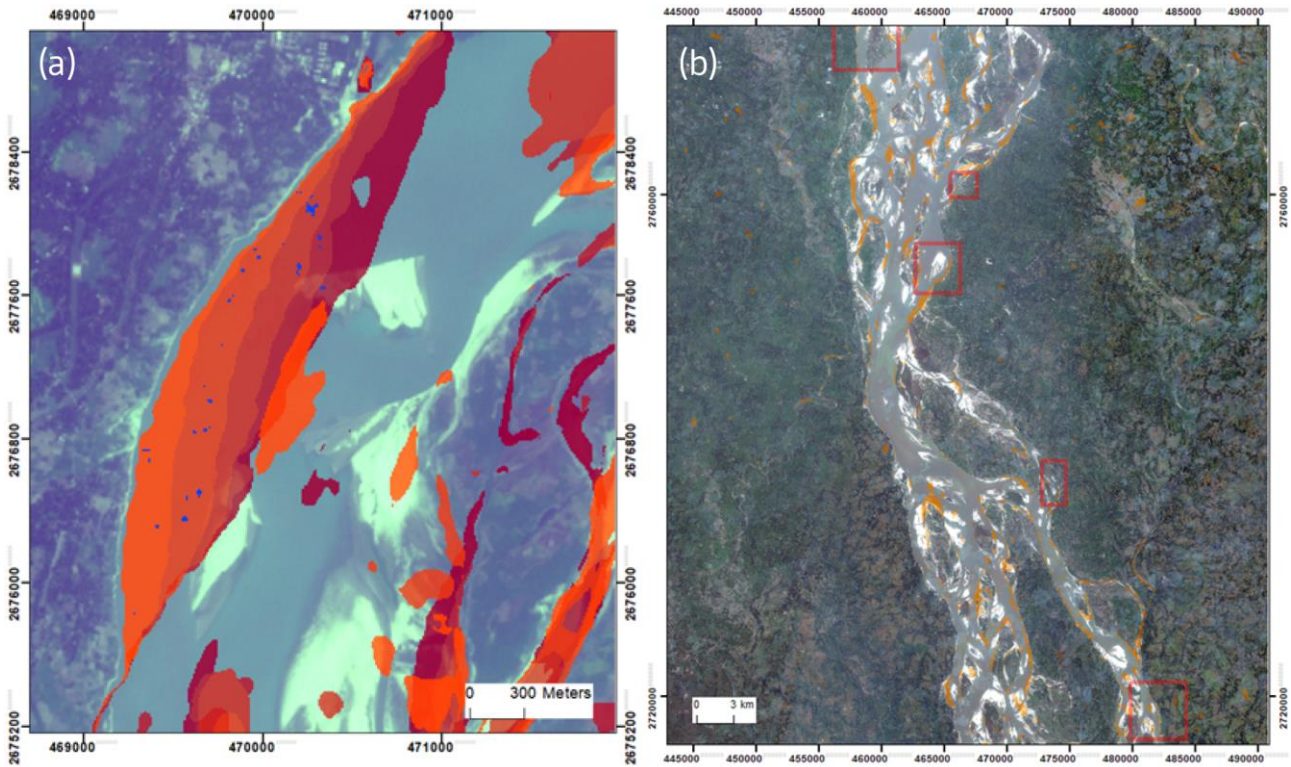
**Figure 9: (a) Detected erosion for the monsoon seasons 2015 (dark red) to 2019 (light red). Blue: eroded settlements. (b) Locations of land eroded during the 2019 monsoon (orange). The red rectangles are the locations for which CEGIS (2018) predicted severe erosion. Source of optical background images: Sentinel-2.**

### 3.4 Accuracy assessment

A confusion matrix of vegetation versus sand/water was calculated for six different months (Table B6). The accuracy metrics were averaged over three consecutive years for both November and March (Table 2). The classification showed a satisfactory accuracy over 87 %. The observed errors might be introduced by the cloud mask which is applied to the Sentinel-2 images and potentially leads to misclassified pixels.

**Table 2: Accuracy assessment of the SAR-based classification for two months. Indicated are the accuracy values averaged for November/March over three consecutive years, respectively.**

| Month | Class | User's accuracy [%] | Producer's accuracy [%] | Overall accuracy [%] |
|-------|-------|---------------------|-------------------------|----------------------|
| November | Sand/water | 94.7 | 83.1 | 87.5 |
| | Vegetation | 80.1 | 93.8 | |
| March | Sand/water | 87.5 | 93.6 | 90.6 |
| | Vegetation | 93.7 | 88.1 | |

As mentioned in Sect. 2.6, a validation based on ground-truth data was not possible due to the large size of our study area. Readers and users are, however, invited to access the source code in the GEE and compare the SAR-based land cover classification to optical imagery for specific sites of interest.

### 3.5 Final implementation

Finally, the results from Sect. 3.1 to 3.3 were implemented in a GEE-based analysis tool that allows the user to explore where erosion of farmland and settlement has occurred during the five monsoon seasons from 2015 to 2019. The tool contains the following information:

- Five layers for land eroded in the five monsoon seasons, 2015 to 2019
- Five layers for settlements eroded in the five monsoon seasons, 2015 to 2019
- One layer for the settlement detected in the beginning of 2020
385
- Three optical images from January 2018, 2019 and 2020 as a visual baseline
- The 14 "erosion hotspots" identified by CEGIS in their 2019 erosion prediction (cf. Sect. 1)

The GEE-based tool to assess riverbank erosion using Sentinel-1 data, as well as a short video tutorial to introduce users who are unfamiliar with the GEE into the application of this tool are referenced in the section "Code availability".

## 4 Discussion

390   Various studies have investigated riverbank erosion along the Jamuna applying remote sensing approaches (Hassan et al., 2017; Khan et al., 2022; Pahlowan and Hossain, 2015; Islam, 2009). All of them, however, used optical images, which are available only at cloudfree daylight conditions. Our study is the first to assess riverbank erosion along the Jamuna using radar satellite images, which are independent of daylight or weather conditions. Hence, they are more readily available after the end of the monsoon season and thus better suited to inform practitioners who are supporting local
395   communities to prepare for the upcoming monsoon and erosion season. In terms of accuracy, our algorithm performed satisfactorily when compared to an approach based on optical images (see Sect. 3.4).

Still, different limitations might affect the results of this study. First, as outlined in Sect. 2.1, the GEE contains only the amplitude, but not the phase values of radar images. The phase value contains information on the distance between the sensor and the ground, accurate to a small fraction of the radar wavelength. One powerful technique employing the phase
400   value is SAR interferometry which compares for one scene the phase of two or more radar images acquired from different positions or at different times (Moreira et al., 2013). Accessing the phase information could thus open up alternative strategies to detect eroded land, for instance from phase decorrelation. SAR interferometry, however, requires special software, which might not be available in resource-constrained settings. The GEE, by contrast, is easy and free to use, making the developed algorithm accessible to authorities and researchers in Bangladesh.

405   Second, our study used only radar data. Combining optical and SAR data generally yields an improved performance compared to using any of the two alone. Examples using both data types include land cover classification (Carrasco et al., 2019; Miettinen et al., 2019; Poortinga et al., 2019; Zhang et al., 2018), change detection (Canty and Nielsen, 2017; Celik, 2018; Shimizu et al., 2019) and the derivation of river discharge for the Upper Brahmaputra River (Huang et al., 2018). The GEE facilitates the combination of optical and SAR data. Such a combination would thus be another strategy
410   to further improve the results of this study.

Third, we have developed the algorithm to detect riverbank erosion for one specific case study. As it is usually the case for case study research, it is not evident how well our findings can be transferred to other contexts beyond Bangladesh. Given, however, that the basic mechanism of riverbank erosion (vegetated/settlement land turning into sand/water) is identical irrespective of where erosion occurs, we believe that it is possible to apply our erosion detection approach to
415   other contexts at relatively low effort (e.g. by adapting classification thresholds to local vegetation/soil types). We invite interested readers – both from research and from practice – to access our algorithm and to apply it to other geographical settings.

# 5 Conclusions

We have implemented and applied a GEE-based method to quantitively assess riverbank erosion along the Jamuna River in Bangladesh based on Sentinel-1 GRD intensity data. Timely detection of riverbank erosion is an essential element of disaster risk management, yet especially challenging in resource-limited settings.

We investigated whether the locations of past erosion events can be extracted from Sentinel-1 SAR imagery. We developed an algorithm to classify land cover, identify settlements and detect eroded farmland and settlements along the Jamuna River. The SAR-based classification approach can provide information on where land and settlements have been eroded during the last monsoon already one month after the end of the monsoon season, and hence potentially earlier or at least more reliably than using optical satellite images, which depend on cloud-free conditions. This erosion detection can be achieved at sufficiently high spatial resolution. We could thus demonstrate the suitability of radar imagery to assess past erosion events.

The analysis was performed using the GEE which gives access to Google's cloud computing infrastructure as well as to massive amounts of satellite imagery, including time series of Sentinel-1 GRD backscatter data and Sentinel-2 optical data on a global scale. A limitation of using the GEE is that it contains only the amplitude-, and not the phase-values of the radar images. Landcover-change classification approaches using interferometric coherence can thus not be implemented in the GEE. However, the GEE facilitates sharing and re-using algorithms, making the results of this study accessible and useable for government agencies or NGOs in Bangladesh. To share our results, we developed an interactive online tool allowing the user to explore where farmland and settlement have eroded along the Jamuna River in the monsoon seasons 2015 to 2019. This online tool as well as the underlying source code can be accessed and adapted free of charge, making it an attractive tool to use in resource-constrained settings.

Spatio-temporally consistent sequences of progressive riverbank erosion give valuable insights on where erosion will likely occur in the following monsoon season. Such information can be used to alert potentially affected residents accordingly. Likewise, the results of our study can be used to inform researchers or NGOs working on the adaptation of the population living along the Jamuna to the riverbank erosion. As such, the tool developed in this study might be of interest to both policymakers and practitioners working in the fields of disaster risk management and communication. Since riverbank erosion is a phenomenon occurring along many of the world's major rivers (e.g. Mekong River, Yellow River, Mississippi River or Danube River), the relevance of our tool extends beyond the specific case study of Bangladesh. Likewise, it might be applicable to coastal erosion – another environmental hazard that is bound to increase in the age of climate change.
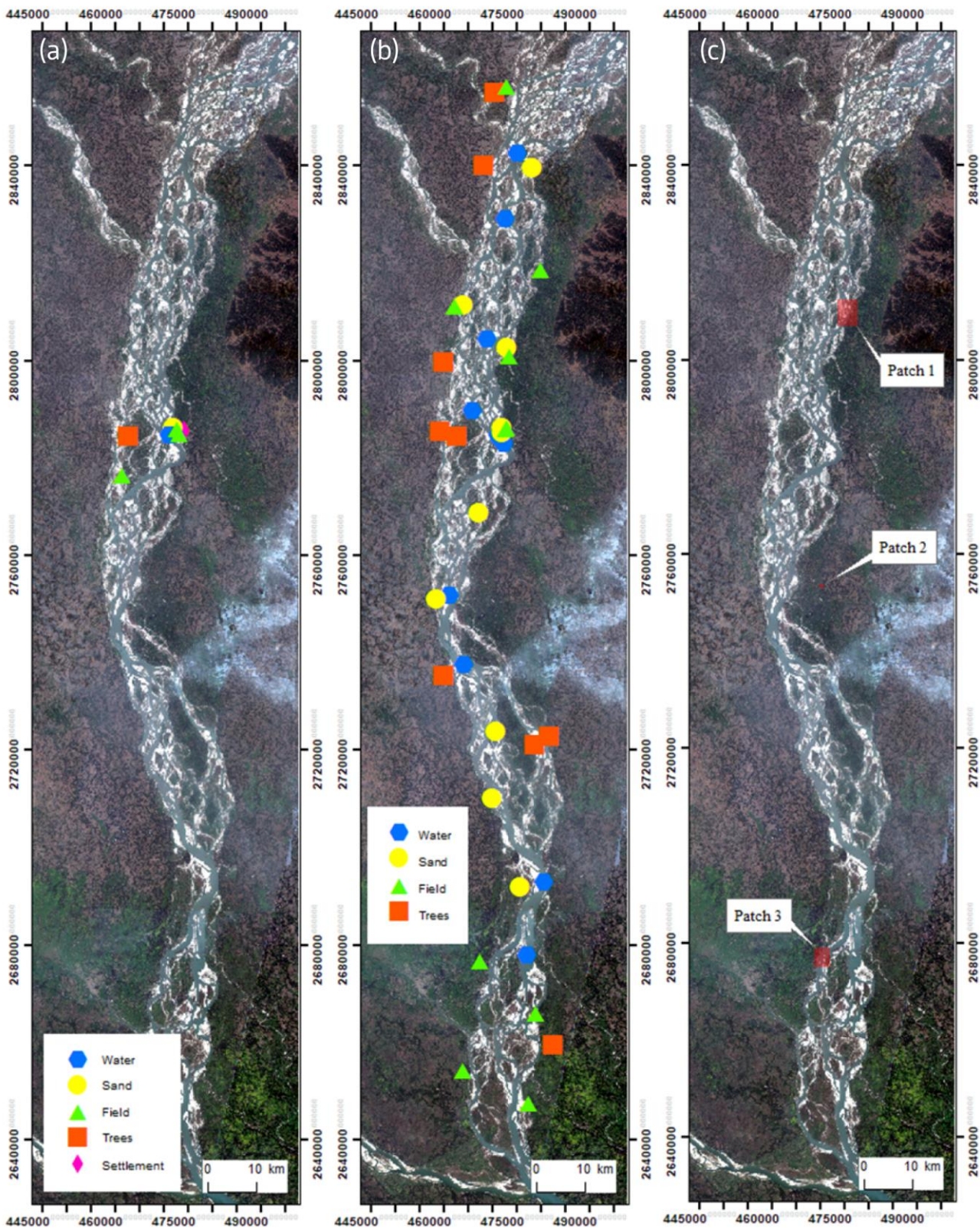
**Figure A1: (a) Locations of the patches shown in Fig. 3 (symbols are larger than the patches). (b) Locations of the patches analyzed for the development of the land cover classification (symbols are larger than the patches). (c) Locations of the patches used to validate the land cover classification (patch 1), the settlement detection (patch 2) and the erosion detection (patch 3). Exact coordinates for all patches are contained in the GEE source code. Source of optical background image: Sentinel-2.**

450
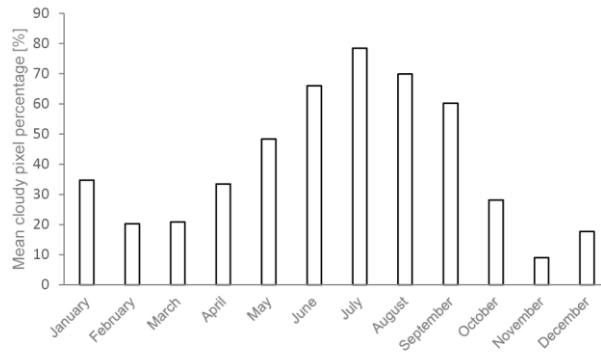
455

**Figure A2: Mean cloudy pixel percentage of all Sentinel-2 images taken over the assessment site during the respective month. For each month, five consecutive years were analysed. The plotted values represent the average of these five years.**

(a)

(b)

(c)

(d)

(e)

(f)

■ Not filtered ■ 3x3 Lee ■ 3x3 Box ■ 5x5 Box ■ 7x7 Box ■ 25x25 Box ■ 50x50 Box
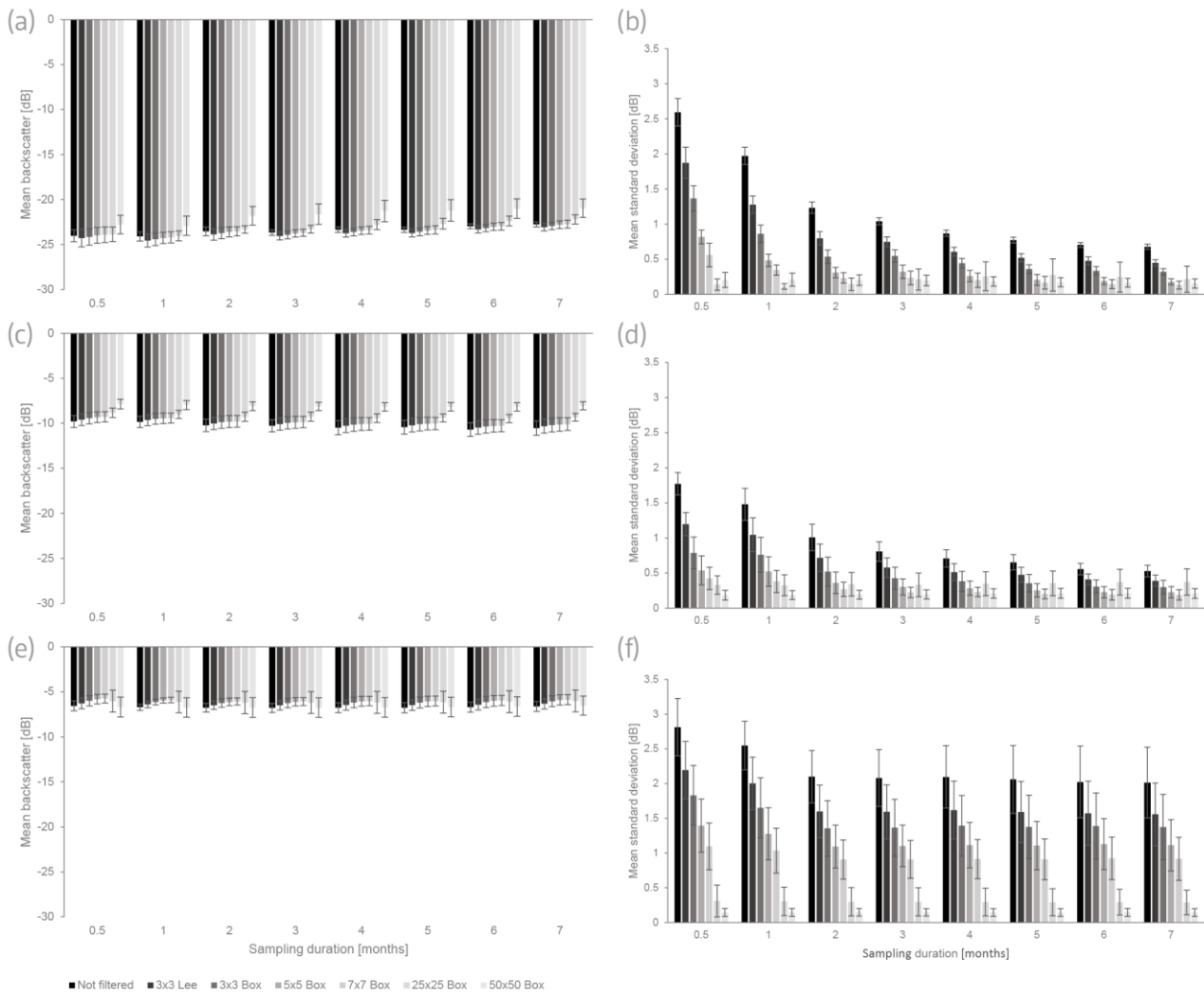
460 **Figure A3: Average backscatter (panels (a), (c) and (e)) and average standard deviation (panels (b), (d) and (f)) of the pixels within ten patches of water (panels (a) and (b)), fields (panels (c) and (d)) and trees (panels (e) and (f)) for different sampling durations and filter sizes. Bars indicate the 95 % confidence interval. Lee – Lee filter. Box – boxcar filter.**
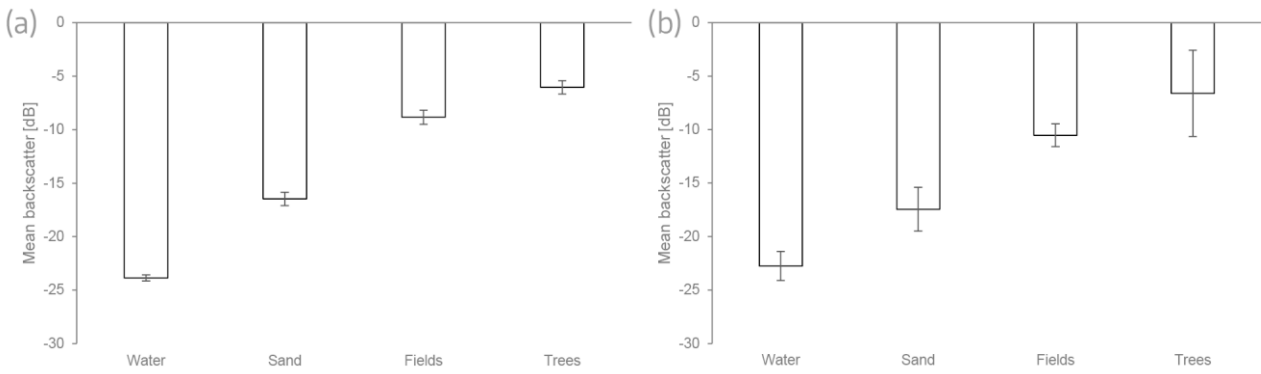
**Figure A4: Average backscatter for four land cover classes (a) for a sampling duration of 0.5 months and a 25x25 boxcar filter and (b) for a sampling duration of 7 months and no filter. Bars indicate the mean ± 2 standard deviations. If images are available only from two weeks, strong spatial filtering (25x25 pixels) reduces the standard deviation enough to separate all four classes even at the level of two standard deviations around the mean (panel (a)). If, by contrast, images are available from seven months, water, sand and fields can be separated even if no spatial filter is applied (panel (b)). In this setting, fields and trees can be distinguished only at the level of one standard deviation around the mean (not shown in the graph).**
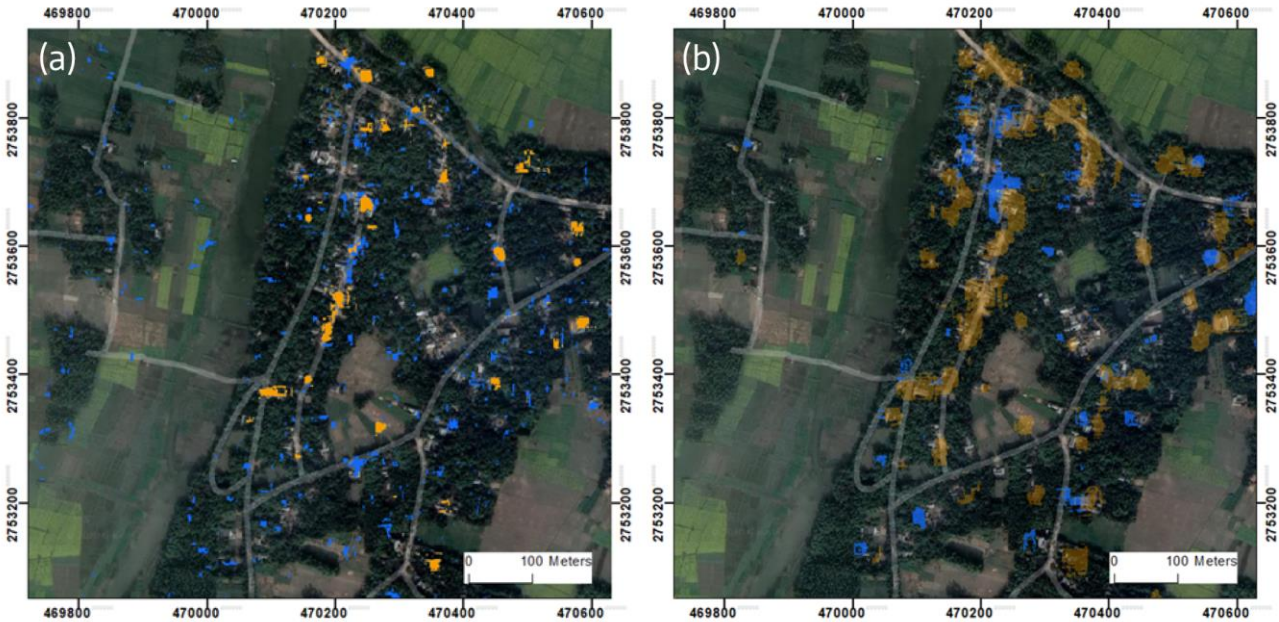
**Figure A5: (a) Classification of settlements using the dispersion index only (blue) or the combination of dispersion index and amplitude threshold (orange). Thresholds: 0.25 (dispersion index), -2 dB (amplitude). (b) Settlement detection for ascending (orange) and descending (blue) orbit. Thresholds: 0.4 (dispersion index), -4 dB (amplitude). Sampling duration for both panels: six months. The location of the patch is shown in Fig. A1 (patch 2). Source of optical background image: Google, ©2020 Maxar Technologies, CNES/Airbus.**

# Appendix B: Additional tables

**Table B1: Determination of thresholds for a sampling duration of six months and a 7x7 boxcar filter. Values in bold are those that have been used to calculate the threshold indicated in the last column. All values are in dB. μ – mean. σ – standard deviation.**

| | μ | σ | μ+σ | μ-σ | μ+2*σ | μ-2*σ | μ+3*σ | μ-3*σ | Threshold |
|---|---|---|---|---|---|---|---|---|---|
| Water | -23.0 | 0.1 | -22.8 | | -22.7 | | **-22.5** | | |
| Sand | -16.9 | 0.4 | -16.5 | -17.3 | -16.0 | -17.7 | **-15.6** | **-18.2** | -20.4 |
| Fields | -10.3 | 0.2 | -10.1 | -10.5 | -9.9 | -10.6 | **-9.7** | **-10.8** | -13.2 |
| Trees | -6.0 | 0.9 | | -6.9 | | -7.8 | | **-8.7** | -9.2 |

480

**Table B2: Determination of thresholds for a sampling duration of one month and a 7x7 boxcar filter. Values in bold are those that have been used to calculate the threshold indicated in the last column. All values are in dB. μ – mean. σ – standard deviation.**

| | μ | σ | μ+σ | μ-σ | μ+2*σ | μ-2*σ | μ+3*σ | μ-3*σ | Threshold |
|---|---|---|---|---|---|---|---|---|---|
| Water | -24.2 | 0.3 | -23.9 | | -23.5 | | **-23.2** | | |
| Sand | -17.1 | 0.7 | -16.3 | -17.8 | -15.6 | -18.5 | **-14.9** | **-19.2** | -21.2 |
| Fields | -9.4 | 0.4 | -9.0 | -9.8 | **-8.7** | -10.2 | -8.3 | **-10.6** | -12.7 |
| Trees | -5.9 | 1.0 | | -6.9 | | **-8.0** | | -9.0 | -8.3 |

485

**Table B3: Determination of thresholds for a sampling duration of two weeks and a 25x25 boxcar filter. Values in bold are those that have been used to calculate the threshold indicated in the last column. All values are in dB. μ – mean. σ – standard deviation.**

| | μ | σ | μ+σ | μ-σ | μ+2*σ | μ-2*σ | μ+3*σ | μ-3*σ | Threshold |
|---|---|---|---|---|---|---|---|---|---|
| Water | -23.9 | 0.1 | -23.7 | | -23.6 | | **-23.4** | | |
| Sand | -16.5 | 0.3 | -16.2 | -16.8 | -15.9 | -17.1 | **-15.5** | **-17.4** | -20.4 |
| Fields | -8.8 | 0.3 | -8.5 | -9.2 | -8.2 | -9.5 | **-7.9** | **-9.8** | -12.7 |
| Trees | -6.0 | 0.3 | | -6.4 | | -6.7 | | **-7.0** | -7.4 |

490

**Table B4: Determination of thresholds for a sampling duration of seven months, unfiltered. Values in bold are those that have been used to calculate the threshold indicated in the last column. All values are in dB. μ – mean. σ – standard deviation.**

| | μ | σ | μ+σ | μ-σ | μ+2*σ | μ-2*σ | μ+3*σ | μ-3*σ | Threshold |
|---|---|---|---|---|---|---|---|---|---|
| Water | -22.8 | 0.7 | -22.1 | | -21.4 | | **-20.7** | | |
| Sand | -17.4 | 1.0 | -16.4 | -18.5 | -15.4 | -19.5 | **-14.4** | **-20.5** | -20.6 |
| Fields | -10.5 | 0.5 | **-10.0** | -11.1 | -9.5 | -11.6 | -8.9 | **-12.1** | -13.2 |
| Trees | -6.6 | 2.0 | | **-8.6** | | -10.6 | | -12.7 | -9.3 |

**Table B5: Average backscatter values from Ulaby and Dobson (1989) for C-band at VV polarization for look angles of 30° and 45°.**

| | 30° | 45° |
|---|---|---|
| Soil and rock | -10.3 | -13.3 |
| Grasses | -10.7 | -14.5 |
| Shrubs | -9.7 | -11.0 |
| Short vegetation | -10.0 | -13.2 |

| | | | | | | |
|---|---|---|---|---|---|---|
| Trees | | -10.8 (for 20°) | | -2.3 | | |

**Table B6: Confusion matrix of resultant land cover classification as obtained from SAR versus Sentinel-2 (S2) for six different months.**

| Month | Class | Sand/water (SAR) [km²] | Vegetation (SAR) [km²] | User's accuracy [%] | Producer's accuracy [%] | Overall accuracy [%] |
|---|---|---|---|---|---|---|
| Nov 18 | Sand/water (S2) | 10.79 | 1.39 | 93.8 | 88.6 | 91.3 |
| | Vegetation (S2) | 0.71 | 11.13 | 88.9 | 94.0 | |
| Nov 19 | Sand/water (S2) | 11.78 | 2.06 | 96.4 | 85.1 | 89.6 |
| | Vegetation (S2) | 0.44 | 9.78 | 82.6 | 95.7 | |
| Nov 20 | Sand/water (S2) | 11.49 | 3.69 | 93.9 | 75.7 | 81.6 |
| | Vegetation (S2) | 0.74 | 8.11 | 68.7 | 91.6 | |
| Mar 19 | Sand/water (S2) | 9.97 | 0.48 | 85.8 | 95.4 | 91.1 |
| | Vegetation (S2) | 1.65 | 11.94 | 96.1 | 87.9 | |
| Mar 20 | Sand/water (S2) | 11.02 | 0.82 | 87.7 | 93.1 | 90.2 |
| | Vegetation (S2) | 1.54 | 10.67 | 92.9 | 87.4 | |
| Mar 21 | Sand/water (S2) | 10.92 | 0.92 | 89.1 | 92.2 | 90.6 |
| | Vegetation (S2) | 1.34 | 10.85 | 92.2 | 89.0 | |

**Code availability**

The GEE code underlying the analyses of this paper is publicly available: doi:10.5281/zenodo.7253121 (or directly in the GEE: https://code.earthengine.google.com/a2a7614af421261a4b639a1abbb609c6).

The interactive online tool implementing the findings of this paper can be accessed here: doi:10.5281/zenodo.7252970 (or directly in the GEE: https://code.earthengine.google.com/b1ba16d48320a3501e89135679d97492?hideCode=true).

To introduce users who are unfamiliar with the GEE into the application of this tool, we have recorded a short tutorial: doi:10.5281/zenodo.7249809 (or directly: youtu.be/_b9AAPDw7Wk).

**Author contribution**

JF and OF jointly conceptualized the overarching research objective and developed the methodology. JF implemented the code and prepared the manuscript with contributions from OF.

**Competing interests**

The authors declare that they have no conflict of interest.

**Acknowledgments**

We would like to thank Thomas Bernauer and Vally Koubi for helpful feedback on earlier drafts of this manuscript. Further, we would like to express our gratitude to Sudipta Hore for providing insightful background information about the erosion prediction prepared by CEGIS. Copernicus Sentinel data 2014-2021, processed by ESA.

**6 References**

Al Fugura, A., Billa, L., and Pradhan, B.: Semi-automated procedures for shoreline extraction using single RADARSAT-1 SAR image, Estuarine, Coastal and Shelf Science, 95, 395–400, https://doi.org/10.1016/j.ecss.2011.10.009, 2011.

520 Alam, G. M. M.: Livelihood Cycle and Vulnerability of Rural Households to Climate Change and Hazards in Bangladesh, Environmental management, 59, 777–791, https://doi.org/10.1007/s00267-017-0826-3, 2017.

Alam, G. M. M., Alam, K., Mushtaq, S., Sarker, M. N. I., and Hossain, M.: Hazards, food insecurity and human displacement in rural riverine Bangladesh: Implications for policy, International Journal of Disaster Risk Reduction, 101364, https://doi.org/10.1016/j.ijdrr.2019.101364, available at:

525 http://www.sciencedirect.com/science/article/pii/S2212420918309361, 2019.

Cable, J., Kovacs, J., Shang, J., and Jiao, X.: Multi-Temporal Polarimetric RADARSAT-2 for Land Cover Monitoring in Northeastern Ontario, Canada, Remote Sensing, 6, 2372–2392, https://doi.org/10.3390/rs6032372, 2014.

Canty, M. J. and Nielsen, A. A.: Spatio-temporal analysis of change with sentinel imagery on the Google Earth Engine, in: ESA Conference on Big Data from Space (BiDS), 126–129, 2017.

530 Carrasco, L., O'Neil, A., Morton, R., and Rowland, C.: Evaluating Combinations of Temporally Aggregated Sentinel-1, Sentinel-2 and Landsat 8 for Land Cover Mapping with Google Earth Engine, Remote Sensing, 11, 288, https://doi.org/10.3390/rs11030288, 2019.

CEGIS: Update, improve and extend the erosion forecasting and warning tools in the three main rivers, Center for Environment and Geographic Information Services, Dhaka, Bangladesh, 2018.

535 Celik, N.: Change Detection of Urban Areas in Ankara through Google Earth Engine, in: 2018 41st International Conference on Telecommunications and Signal Processing (TSP), Athens, Greece, 7/4/2018 - 7/6/2018, 1–5, 2018.

Chu, Z. X., Sun, X. G., Zhai, S. K., and Xu, K. H.: Changing pattern of accretion/erosion of the modern Yellow River (Huanghe) subaerial delta, China: Based on remote sensing images, Marine Geology, 227, 13–30, https://doi.org/10.1016/j.margeo.2005.11.013, 2006.

540 Chung, H.-W., Liu, C.-C., Cheng, I.-F., Lee, Y.-R., and Shieh, M.-C.: Rapid Response to a Typhoon-Induced Flood with an SAR-Derived Map of Inundated Areas: Case Study and Validation, Remote Sensing, 7, 11954–11973, https://doi.org/10.3390/rs70911954, 2015.

DeFries, R. S. and Townshend, J. R. G.: NDVI-derived land cover classifications at a global scale, International Journal of Remote Sensing, 15, 3567–3586, https://doi.org/10.1080/01431169408954345, 1994.

545 Dixon, S. J., Sambrook Smith, G. H., Best, J. L., Nicholas, A. P., Bull, J. M., Vardy, M. E., Sarker, M. H., and Goodbred, S.: The planform mobility of river channel confluences: Insights from analysis of remotely sensed imagery, Earth-Science Reviews, 176, 1–18, https://doi.org/10.1016/j.earscirev.2017.09.009, 2018.

Donovan, M., Belmont, P., Notebaert, B., Coombs, T., Larson, P., and Souffront, M.: Accounting for uncertainty in remotely-sensed measurements of river planform change, Earth-Science Reviews, 193, 220–236,

550 https://doi.org/10.1016/j.earscirev.2019.04.009, 2019.

Du, Y., Zhang, Y., Ling, F., Wang, Q., Li, W., and Li, X.: Water Bodies' Mapping from Sentinel-2 Imagery with Modified Normalized Difference Water Index at 10-m Spatial Resolution Produced by Sharpening the SWIR Band, Remote Sensing, 8, 354, https://doi.org/10.3390/rs8040354, 2016.

El-Behaedi, R. and Ghoneim, E.: Flood risk assessment of the Abu Simbel temple complex (Egypt) based on high-

555 resolution spaceborne stereo imagery, Journal of Archaeological Science: Reports, 20, 458–467, https://doi.org/10.1016/j.jasrep.2018.05.019, 2018.

ESA: Sentinel-1 SAR. Acquisition modes, https://sentinel.esa.int/web/sentinel/user-guides/sentinel-1-sar/acquisition-modes, 2020a.

ESA: Sentinel-1. Mission summary, European Space Agency, https://sentinel.esa.int/web/sentinel/missions/sentinel-1/overview/mission-summary, 2020b.

560

ESA: Sentinel-2, European Space Agency, https://sentinel.esa.int/web/sentinel/missions/sentinel-2, 2020c.

Ferdous, M. R., Wesselink, A., Brandimarte, L., Slager, K., Zwarteveen, M., and Di Baldassarre, G.: The Costs of Living with Floods in the Jamuna Floodplain in Bangladesh, Water, 11, 1238, https://doi.org/10.3390/w11061238, 2019.

565

Ferretti, A., Prati, C., and Rocca, F.: Permanent scatterers in SAR interferometry, IEEE Trans. Geosci. Remote Sensing, 39, 8–20, https://doi.org/10.1109/36.898661, 2001.

Ferretti, A., Prati, C., and Rocca, F.: Permanent scatterers in SAR interferometry, in: IEEE 1999 International Geoscience and Remote Sensing Symposium. IGARSS'99 (Cat. No.99CH36293), Hamburg, Germany, 28 June-2 July 1999, 1528–1530, 1999.

570

Google Developers: Sentinel-1 Algorithms, https://developers.google.com/earth-engine/sentinel1, 2020.

Gorelick, N., Hancher, M., Dixon, M., Ilyushchenko, S., Thau, D., and Moore, R.: Google Earth Engine: Planetary-scale geospatial analysis for everyone, Remote Sensing of Environment, 202, 18–27, https://doi.org/10.1016/j.rse.2017.06.031, available at: http://www.sciencedirect.com/science/article/pii/S0034425717302900, 2017.

575

Hassan, M. A., Ratna, S. J., Hassan, M., and Tamanna, S.: Remote Sensing and GIS for the Spatio-Temporal Change Analysis of the East and the West River Bank Erosion and Accretion of Jamuna River (1995-2015), Bangladesh, GEP, 05, 79–92, https://doi.org/10.4236/gep.2017.59006, 2017.

Hossain, M. A., Gan, T. Y., and Baki, A. B. M.: Assessing morphological changes of the Ganges River using satellite images, Quaternary International, 304, 142–155, https://doi.org/10.1016/j.quaint.2013.03.028, 2013.

580

Huang, C., Zhang, C., He, Y., Liu, Q., Li, H., Su, F., Liu, G., and Bridhikitti, A.: Land Cover Mapping in Cloud-Prone Tropical Areas Using Sentinel-2 Data: Integrating Spectral Features with Ndvi Temporal Dynamics, Remote Sensing, 12, 1163, https://doi.org/10.3390/rs12071163, 2020.

Huang, Q., Di Long, Du, M., Zeng, C., Qiao, G., Li, X., Hou, A., and Hong, Y.: Discharge estimation in high-mountain regions with improved methods using multisource remote sensing: A case study of the Upper Brahmaputra River,

585

Remote Sensing of Environment, 219, 115–134, https://doi.org/10.1016/j.rse.2018.10.008, 2018.

Imhoff, M. L., Vermillion, C., Story, M. H., Choudhury, A. M., Gafoor, A., and Polcyn, F.: Monsoon flood boundary delineation and damage assessment using space borne imaging radar and Landsat data, Photogrammetric Engineering and Remote Sensing, 53, 405–413, 1987.

Immitzer, M., Vuolo, F., and Atzberger, C.: First Experience with Sentinel-2 Data for Crop and Tree Species Classifications in Central Europe, Remote Sensing, 8, 166, https://doi.org/10.3390/rs8030166, 2016.

590

Islam, M. T.: Quantification of eroded and deposited riverbanks and monitoring river's channel using RS and GIS, in: 2009 17th International Conference on Geoinformatics, Fairfax, VA, 8/12/2009 - 8/14/2009, 1–5, 2009.

Islam, M. S. and Matin, M. A.: Prediction of fluvial erosion rate in Jamuna River, Bangladesh, International Journal of River Basin Management, 1–13, https://doi.org/10.1080/15715124.2022.2068561, 2022.

595

Joyce, K. E., Dellow, G. D., and Glassey, P. J.: Using remote sensing and spatial analysis to understand landslide distribution and dynamics in New Zealand, in: 2009 IEEE International Geoscience and Remote Sensing Symposium, Cape Town, South Africa, 7/12/2009 - 7/17/2009, III-224-III-227, 2009.

Kampes, B. M. and Adam, N.: Deformation parameter inversion using permanent scatterers in interferogram time series, European Conference on Synthetic Aperture Radar, Ulm, Germany, 25–27 May 2004, 2004.

600     Khan, N. S., Roy, S. K., Mazumder, M. T. R., Talukdar, S., and Mallick, J.: Assessing the long-term planform dynamics of Ganges–Jamuna confluence with the aid of remote sensing and GIS, Nat Hazards, 114, 883–906, https://doi.org/10.1007/s11069-022-05416-6, 2022.

Kummu, M., Lu, X. X., Rasphone, A., Sarkkula, J., and Koponen, J.: Riverbank changes along the Mekong River: Remote sensing detection in the Vientiane–Nong Khai area, Quaternary International, 186, 100–112,

605     https://doi.org/10.1016/j.quaint.2007.10.015, 2008.

Langendoen, E. J. and Simon, A.: Modeling the Evolution of Incised Streams. II: Streambank Erosion, J. Hydraul. Eng., 134, 905–915, https://doi.org/10.1061/(ASCE)0733-9429(2008)134:7(905), 2008.

Lee, J.-S.: Refined filtering of image noise using local statistics, Computer Graphics and Image Processing, 15, 380–389, https://doi.org/10.1016/S0146-664X(81)80018-4, 1981.

610     Lee, J.-S., Wen, J.-H., Ainsworth, T. L., Chen, K.-S., and Chen, A. J.: Improved Sigma Filter for Speckle Filtering of SAR Imagery, IEEE Trans. Geosci. Remote Sensing, 47, 202–213, https://doi.org/10.1109/TGRS.2008.2002881, 2009.

Liu, C.-C., Shieh, M.-C., Ke, M.-S., and Wang, K.-H.: Flood Prevention and Emergency Response System Powered by Google Earth Engine, Remote Sensing, 10, 1283, https://doi.org/10.3390/rs10081283, 2018.

615     Luppi, L., Rinaldi, M., Teruggi, L. B., Darby, S. E., and Nardi, L.: Monitoring and numerical modelling of riverbank erosion processes: a case study along the Cecina River (central Italy), Earth Surface Processes and Landforms, 34, 530–546, https://doi.org/10.1002/esp.1754, 2009.

Mandal, D., Kumar, V., Bhattacharya, A., Rao, Y. S., Siqueira, P., and Bera, S.: Sen4Rice: A Processing Chain for Differentiating Early and Late Transplanted Rice Using Time-Series Sentinel-1 SAR Data With Google Earth

620     Engine, IEEE Geosci. Remote Sensing Lett., 15, 1947–1951, https://doi.org/10.1109/LGRS.2018.2865816, 2018.

Martinez, J.-M. and Le Toan, T.: Mapping of flood dynamics and spatial distribution of vegetation in the Amazon floodplain using multitemporal SAR data, Remote Sensing of Environment, 108, 209–223, https://doi.org/10.1016/j.rse.2006.11.012, 2007.

Martinis, S., Kersten, J., and Twele, A.: A fully automated TerraSAR-X based flood service, ISPRS Journal of

625     Photogrammetry and Remote Sensing, 104, 203–212, https://doi.org/10.1016/j.isprsjprs.2014.07.014, 2015.

Martinis, S., Twele, A., and Voigt, S.: Towards operational near real-time flood detection using a split-based automatic thresholding procedure on high resolution TerraSAR-X data, Natural Hazards & Earth System Sciences, 9, 2009.

Miettinen, J., Shi, C., and Liew, S. C.: Towards automated 10–30 m resolution land cover mapping in insular South-East Asia, Geocarto International, 34, 443–457, https://doi.org/10.1080/10106049.2017.1408700, 2019.

630     Misachi, J.: Where Is The Largest Delta In The World?, https://www.worldatlas.com/articles/which-is-the-largest-delta-in-the-world.html, last access: 24 October 2022, 2017.

Moreira, A., Prats-Iraola, P., Younis, M., Krieger, G., Hajnsek, I., and Papathanassiou, K. P.: A tutorial on synthetic aperture radar, IEEE Geosci. Remote Sens. Mag., 1, 6–43, https://doi.org/10.1109/MGRS.2013.2248301, 2013.

Mount, N. J., Tate, N. J., Sarker, M. H., and Thorne, C. R.: Evolutionary, multi-scale analysis of river bank line retreat

635     using continuous wavelet transforms: Jamuna River, Bangladesh, Geomorphology, 183, 82–95, https://doi.org/10.1016/j.geomorph.2012.07.017, 2013.

Muro, J., Strauch, A., Fitoka, E., Tompoulidou, M., and Thonfeld, F.: Mapping Wetland Dynamics With SAR-Based Change Detection in the Cloud, IEEE Geosci. Remote Sensing Lett., 16, 1536–1539, https://doi.org/10.1109/LGRS.2019.2903596, 2019.

640    Oberhagemann, K., Haque, A. M. A., and Thompson, A.: A Century of Riverbank Protection and River Training in Bangladesh, Water, 12, 3018, https://doi.org/10.3390/w12113018, 2020.

Pahlowan, E. U. and Hossain, A. S.: Jamuna River Erosional Hazards, Accretion & Annual Water Discharge – A Remote Sensing & Gis Approach, Int. Arch. Photogramm. Remote Sens. Spatial Inf. Sci., XL-7/W3, 831–835, https://doi.org/10.5194/isprsarchives-XL-7-W3-831-2015, 2015.

645    Poortinga, A., Tenneson, K., Shapiro, A., Nquyen, Q., San Aung, K., Chishtie, F., and Saah, D.: Mapping Plantations in Myanmar by Fusing Landsat-8, Sentinel-2 and Sentinel-1 Data along with Systematic Error Quantification, Remote Sensing, 11, 831, https://doi.org/10.3390/rs11070831, 2019.

Rishikeshan, C. A. and Ramesh, H.: An automated mathematical morphology driven algorithm for water body extraction from remotely sensed images, ISPRS Journal of Photogrammetry and Remote Sensing, 146, 11–21,
650    https://doi.org/10.1016/j.isprsjprs.2018.08.014, 2018.

Santoro, M. and Wegmuller, U.: Multi-temporal Synthetic Aperture Radar Metrics Applied to Map Open Water Bodies, IEEE J. Sel. Top. Appl. Earth Observations Remote Sensing, 7, 3225–3238, https://doi.org/10.1109/JSTARS.2013.2289301, 2014.

Sarker, M. H., Thorne, C. R., Aktar, M. N., and Ferdous, M. R.: Morpho-dynamics of the Brahmaputra–Jamuna River,
655    Bangladesh, Geomorphology, 215, 45–59, https://doi.org/10.1016/j.geomorph.2013.07.025, 2014.

Sghaier, M. O., Foucher, S., and Lepage, R.: River Extraction From High-Resolution SAR Images Combining a Structural Feature Set and Mathematical Morphology, IEEE J. Sel. Top. Appl. Earth Observations Remote Sensing, 10, 1025–1038, https://doi.org/10.1109/JSTARS.2016.2609804, 2017.

Shimizu, K., Ota, T., and Mizoue, N.: Detecting Forest Changes Using Dense Landsat 8 and Sentinel-1 Time Series
660    Data in Tropical Seasonal Forests, Remote Sensing, 11, 1899, https://doi.org/10.3390/rs11161899, 2019.

Singha, M., Dong, J., Zhang, G., and Xiao, X.: High resolution paddy rice maps in cloud-prone Bangladesh and Northeast India using Sentinel-1 data, Scientific data, 6, 26, https://doi.org/10.1038/s41597-019-0036-3, 2019.

Townsend, P. A.: Mapping seasonal flooding in forested wetlands using multi-temporal Radarsat SAR, Photogrammetric Engineering and Remote Sensing, 67, 857–864, 2001.

665    Trianni, G., Angiuli, E., Lisini, G., and Gamba, P.: Human settlements from Landsat data using Google Earth Engine, in: 2014 IEEE Geoscience and Remote Sensing Symposium, Quebec City, QC, 7/13/2014 - 7/18/2014, 1473–1476, 2014.

Twele, A., Cao, W., Plank, S., and Martinis, S.: Sentinel-1-based flood mapping: a fully automated processing chain, International Journal of Remote Sensing, 37, 2990–3004, https://doi.org/10.1080/01431161.2016.1192304, 2016.

670    Ulaby, F. T. and Dobson, M. C.: Handbook of radar scattering statistics for terrain, The Artech House remote sensing library, Artech House, Norwood, Mass., 357 pp., 1989.

van Leijen, F. J.: Persistent scatterer interferometry based on geodetic estimation theory, TU Delft, 194 blz. ;, 2014.

Veci, L., Lu, J., Prats-Iraola, P., Scheiber, R., Collard, F., Fomferra, N., and Engdahl, M.: The sentinel-1 toolbox, in: Proceedings of the IEEE International Geoscience and Remote Sensing Symposium (IGARSS), 1–3, 2014.

675    Williams, R. D., Measures, R., Hicks, D. M., and Brasington, J.: Assessment of a numerical model to reproduce event-scale erosion and deposition distributions in a braided river, Water resources research, 52, 6621–6642, https://doi.org/10.1002/2015WR018491, 2016.

Zhang, X., Wu, B., Ponce-Campos, G., Zhang, M., Chang, S., and Tian, F.: Mapping up-to-Date Paddy Rice Extent at 10 M Resolution in China through the Integration of Optical and Synthetic Aperture Radar Images, Remote
680    Sensing, 10, 1200, https://doi.org/10.3390/rs10081200, 2018.